

Physical properties and defect processes of M₃SnC₂ (M = Ti, Zr, Hf) MAX phases: Effect of M-elements

Hadi, M. A., Christopoulos, S., Naqib, S. H., Chroneos, A., Fitzpatrick, M., & Islam, A. K. M. A.

Author post-print (accepted) deposited by Coventry University's Repository

Original citation & hyperlink:

Hadi, MA, Christopoulos, S, Naqib, SH, Chroneos, A, Fitzpatrick, M & Islam, AKMA 2018, 'Physical properties and defect processes of M₃SnC₂ (M = Ti, Zr, Hf) MAX phases: Effect of M-elements' *Journal of Alloys and Compounds*, vol 748, pp. 804-813.

<https://dx.doi.org/10.1016/j.jallcom.2018.03.182>

DOI [10.1016/j.jallcom.2018.03.182](https://doi.org/10.1016/j.jallcom.2018.03.182)

ISSN 0925-8388

Publisher: Elsevier

NOTICE: this is the author's version of a work that was accepted for publication in *Journal of Alloys and Compounds*. Changes resulting from the publishing process, such as peer review, editing, corrections, structural formatting, and other quality control mechanisms may not be reflected in this document. Changes may have been made to this work since it was submitted for publication. A definitive version was subsequently published in *Journal of Alloys and Compounds*, 748, (2018) DOI: [10.1016/j.jallcom.2018.03.182](https://doi.org/10.1016/j.jallcom.2018.03.182)

© 2017, Elsevier. Licensed under the Creative Commons Attribution-NonCommercial-NoDerivatives 4.0 International

<http://creativecommons.org/licenses/by-nc-nd/4.0/>

Copyright © and Moral Rights are retained by the author(s) and/ or other copyright owners. A copy can be downloaded for personal non-commercial research or study, without prior permission or charge. This item cannot be reproduced or quoted extensively from without first obtaining permission in writing from the copyright holder(s). The content must not be changed in any way or sold commercially in any format or medium without the formal permission of the copyright holders.

This document is the author's post-print version, incorporating any revisions agreed during the peer-review process. Some differences between the published version and this version may remain and you are advised to consult the published version if you wish to cite from it.

Physical properties and defect processes of M_3SnC_2 ($M = Ti, Zr, Hf$) MAX phases: Effect of M-elements

M. A. Hadi,^{1*} S.-R. G. Christopoulos,² S. H. Naqib,¹ A. Chroneos,^{2,3*} M. E. Fitzpatrick,² and A. K. M. A. Islam^{1,4}

¹Department of Physics, University of Rajshahi, Rajshahi 6205, Bangladesh

²Faculty of Engineering, Environment and Computing, Coventry University, Priory Street, Coventry CV1 5FB, UK

³Department of Materials, Imperial College, London SW7 2AZ, UK

⁴International Islamic University Chittagong, Kumira, Chittagong-4318, Bangladesh

Abstract

We have employed density functional theory calculations for determining intrinsic defect processes and structural, elastic, and electronic properties of recently synthesized Sn-containing 312 MAX phases M_3SnC_2 ($M = Ti, Zr, Hf$) including Debye temperature, Mulliken populations, theoretical hardness, charge density, and Fermi surface. The calculated lattice parameters justify the reliability of the present investigation, as they agree with the experimental values. The lattice constant a increases as the M-element moves from Ti to Hf in the periodic table. The mechanical stability of these compounds is verified with the computed single crystal elastic constants. Hf-based Hf_3SnC_2 is nearly isotropic elastically in view of the calculated parameters. The Debye temperatures decrease following the sequence of M-element: $Ti \rightarrow Zr \rightarrow Hf$. The investigated band structures indicate that the electrical conduction increases as the M-element moves down from the top of the group in the periodic table. A gradual decrease in electronic density of states (DOS) at E_F also follows the order of M-element in the periodic table. The covalency of M-C bonds is calculated to be increased as M-atoms moves from Ti to Hf via Zr. The rank of machinability for these compounds should be $Zr_3SnC_2 > Hf_3SnC_2 > Ti_3SnC_2$. The Fermi surface topologies of the three 312 MAX phases are almost similar and comparable with those of 211 MAX phase counterparts. Considering defect reaction energies, it can be concluded that Ti_3SnC_2 is predicted to be the most radiation-tolerant among Sn-MAX phases considered.

Keywords: MAX phases; density functional theory; physical properties; defect processes

1. Introduction

The MAX phases have received attention since the discovery of phase pure and dense Ti_3SiC_2 in 1996 [1], though this family of ternary compounds was originally identified in 1960 [2]. Ti_3SiC_2 is a material shows a unique combination of properties usually possessed by either metals or ceramics. Its metal-like properties are high thermal and electrical conductivities, machinability and microscale ductility at room temperature. The ceramic-like properties are low density, elastic rigidity and excellent thermal shock and oxidation resistance. The subsequent discovery of Ti_4AlN_3 indicated that this family of compounds shares a basic structure which is responsible for their uncommon properties [3]. This led to the nomenclature “ $M_{n+1}AX_n$ ” (later abbreviated to MAX) phases, which also reveals the chemical formula for this group of compounds [4]. In this formula, M, A, and X are transition metal, A-group element, and carbon and/or nitrogen, respectively [1,5]. The n -values can classify the MAX phases into different sub-families, namely 211, 312, and 413 phases for $n = 1, 2, \text{ and } 3$, respectively.

The MAX phases crystallize in layered hexagonal structures with space group $P6_3/mmc$ (no. 194). These compounds are composed of alternate near-close-packed layers of M_6X octahedra intercalated with pure A-atomic layers. The M_6X octahedra, close to those forming in the corresponding MX binary phases, are connected to each other by edge sharing [6]. The key difference in the structures of 211, 312, and 413 MAX phases depends on the number of M-layers separating every two A-layers. Actually, in the 211, 312, and 413 phases, two, three, and four M-layers are present in the middle of every two A-layers. Due to such atomic arrangements, the MAX phases possess characteristic layered structures which are responsible for the unusual combination of both metallic and ceramic properties.

* Corresponding authors: hadijab@gmail.com ; alexander.chroneos@imperial.ac.uk

The MAX phases are sometimes termed as ‘metallic ceramics’ as they own properties of metals and ceramics. The MAX phases are also termed as ‘nanolaminates’ due to having effective laminated monolayers [7].

Aryal *et al.* [8] have predicted 665 MAX phases, which are possible to exist physically. Day by day the list of MAX phases increases by the synthesis of new compounds [9-11]. Very recently, Lapauw *et al.* [12] have synthesized three 312 MAX phases in the M-Sn-C systems with M = Ti, Zr, and Hf by reactive spark plasma sintering. By adding Fe, Co or Ni to M-Sn-C mixtures, it has been possible to form 312 phases i.e., Ti_3SnC_2 , Zr_3SnC_2 and Hf_3SnC_2 , though their 211 counterparts are formed without such doping. Among these three MAX phases, Ti_3SnC_2 is the first Sn-containing 312 phase, synthesized in 2007 [13]. The newly synthesized Zr_3SnC_2 and Hf_3SnC_2 , were first predicted in 2014 with a theoretical approach calculating the elastic tensors and electronic structures [8]. Many other physical properties of these two ternaries are still unexplored. In this study, we report a complete assessment on the mechanical properties, elastic Debye temperature, melting point, chemical bonding, theoretical hardness, charge density and Fermi surface for these three Sn-containing 312 MAX phases.

The studied compounds are also verified for using as thermal barrier coating (TBC) materials based on their calculated properties. TBC materials are two layered systems whose top coat is a ceramic layer and the underlying coat is a metallic bonded material layer. The ceramics with relatively high thermal expansion coefficient, low thermal conductivity and high thermal shock resistance are suitable for top-coat materials. For underlying coat, the metallic bonded materials should have low thermal conductivity, good oxidation resistance, high coefficient of thermal expansion, slow rate of growth, adhesive power to be adherent to the thermally grown oxide (TGO), stability and ability to match adequately with the substrate. Phonons are the main contributors to the TBC materials. The role of different phonon modes to TBC in different configurations is important. For example, the low frequency in-plane acoustic modes have the dominant contributions to the TBC in the configurations with low interfacial spacing between graphene and h-BN [**]. Higher phonon frequency corresponds to the lower thermal conductivity. So, in the present study, we have emphasized on thermal conductivity assessed from the calculated Debye temperature to predict the TBC materials.

The arrangement of the rest of this paper is as follows: The computational methods are described briefly in Section 2. The results obtained in this study are explained and compared in Section 3. The concluding remarks are summarized in Section 4.

2. Computational methods

The first-principle plane-wave pseudopotential total energy methods based on density functional theory (DFT) [14,15] are carried out with the CASTEP code [16]. The interactions between electrons and ion cores are treated with the ultrasoft pseudopotential developed by Vanderbilt [17]. The generalized gradient approximation according to Perdew-Burkey-Ernzerhof (GGA-PBE) is used to treat the electronic exchange and correlation potential [18]. For searching the ground state of crystals, the Broyden-Fletcher-Goldfarb-Shanno (BFGS) algorithm is used to minimize the total energy and internal forces [19]. The crystal structures are fully optimized by independently modifying the lattice parameters and internal positions of atoms leaving core correction or spin effect. The Monkhorst-Pack (MP) grid with a special k-point mesh of $17 \times 17 \times 2$ is selected for sampling the Brillouin zone [20]. An energy cutoff of 550 eV is fixed for plane-wave expansion in reciprocal space. In geometry optimization, the stringent convergence criteria are used as 5×10^{-6} eV/atom for the difference in total energy, 0.01 eV/Å for the maximum ionic Hellmann-Feynman force, 5×10^{-4} Å for the maximum ionic displacement, and 0.02 GPa for maximum stress.

The elastic constants are calculated using the DFT-based finite-strain method [21] as implemented in the CASTEP code. According to this method, the resultant stress is calculated with respect to optimizing the internal degrees of freedom after applying a set of finite homogeneous deformations (strains). Then the elastic constants are obtained by solving the equation, $\sigma_{ij} = \sum_{kl} C_{ijkl} \delta_j$, where σ_{ij} is the stress tensor under a set of applied strains δ_j . To calculate the elastic properties, this method has already become successful for many kinds of solid crystals [7,22-33]. The bulk modulus B and shear modulus G are calculated using Voigt-Reuss-Hill approximations [34-36]. The convergence criteria

for elastic properties calculation are set as: the difference in total energy less than 10×10^{-7} eV/atom, the maximum ionic Hellmann-Feynman force less than 2×10^{-3} eV/Å, and the maximum ionic displacement less than 10×10^{-5} Å. Only for Hf_3SnC_2 , a $16 \times 16 \times 2$ k-point mesh is used for elastic calculations. For Fermi surface calculations, a k-point mesh of $26 \times 26 \times 4$ for Hf_3SnC_2 and $24 \times 24 \times 4$ for Ti_3SnC_2 and Zr_3SnC_2 are used to obtain smooth topology.

To perform population analysis, the CASTEP code uses a projection of the planewave states onto a localized (LCAO) basis via a method developed by Sanchez-Portal *et al.* [37]. Population analysis of the resultant projected states is subsequently performed with the Mulliken formalism [38]. The defect calculations were performed a 108-atomic site supercell under constant pressure conditions using a $3 \times 3 \times 1$ MP *k*-point grid. To identify the potential interstitial sites we performed an intensive computational search considering all possible interstitial sites. The defect energies considered are effectively energy differences (refer to defect reactions in section 3.6) between isolated defects. The efficacy of the method to calculate the defect properties and the convergence as compared to experiment has been discussed in recent studies [39-41].

3. Results and discussions

3.1. Structural properties

Like all other MAX phases, Ti_3SnC_2 , Zr_3SnC_2 and Hf_3SnC_2 crystallize in the hexagonal structure with space group $P6_3/mmc$ (No. 194). Few 312 MAX phases have been identified with two polymorphic structures in the same space group [42-44]. Polymorphism in this sub-family can be traced to the A-group element residing in the different internal sites in the unit cell, with the MX-slabs remaining unchanged [42-45]. In the α -polymorphic structure, the A-atom resides in a $2b$ Wyckoff site with fractional coordinates (0, 0, 1/4), whereas in β -polymorphic structure, the A-atom resides in a $2d$ Wyckoff position with fractional coordinates (2/3, 1/3, 1/4). The first Sn-containing 312 MAX phase Ti_3SnC_2 crystallize with α -polymorphic structure [13] and a theoretical study suggests that α - Ti_3SnC_2 is more energetically favorable than β - Ti_3SnC_2 [46]. The newly synthesized Zr_3SnC_2 and Hf_3SnC_2 also crystallize with an α -polymorphic structure [12]. So, we restrict our calculations only for α -polymorphic structure of these three Sn-containing 312 MAX phases.

The calculated lattice constants a and c , hexagonal ratio c/a , internal parameters z_{M1} and z_{C} and unit cell volume V are listed in **Table 1**. The experimental values of these parameters for the three 312 phases with Fe as additive and other theoretical values are also listed to make a comparison with them. **Fig. 1** shows the structural parameters obtained in the present study and measured in experiment [12] as a function of M-elements. The calculated lattice constants and unit cell volume agree reasonably with the experimental results with a deviation less than 1.73% for lattice constants and 4.61% for unit cell volume.

Table 1. Structural properties of M_3SnC_2 (M = Ti, Zr, and Hf) MAX phases.

Phases	$a / \text{Å}$	$c / \text{Å}$	c/a	z_{M1}	z_{C}	$V / \text{Å}^3$	Remarks
Ti_3SnC_2	3.1448	18.703	5.9472	0.1243	0.0684	160.2	This Calc.
	3.1500	18.737	5.9483	-----	-----	161.0	Calc. [8]
	3.1173	18.436	5.9140	0.1266	0.0693	155.2	Calc. [46]
	3.1341	18.641	5.9478	-----	-----	158.6	Expt. [12]
	3.1366	18.650	5.9459	0.1204	0.0720	158.9	Expt. [13]
Zr_3SnC_2	3.3693	20.043	5.9486	0.1283	0.0699	197.0	This Calc.
	3.3840	20.080	5.9338	-----	-----	199.1	Calc. [8]
	3.3585	19.876	5.9181	-----	-----	194.2	Expt. [12]
Hf_3SnC_2	3.3733	19.829	5.8783	0.1296	0.0697	195.4	This Calc.
	3.3340	19.775	5.9313	-----	-----	190.4	Calc. [8]
	3.3162	19.611	5.9137	-----	-----	186.8	Expt. [12]

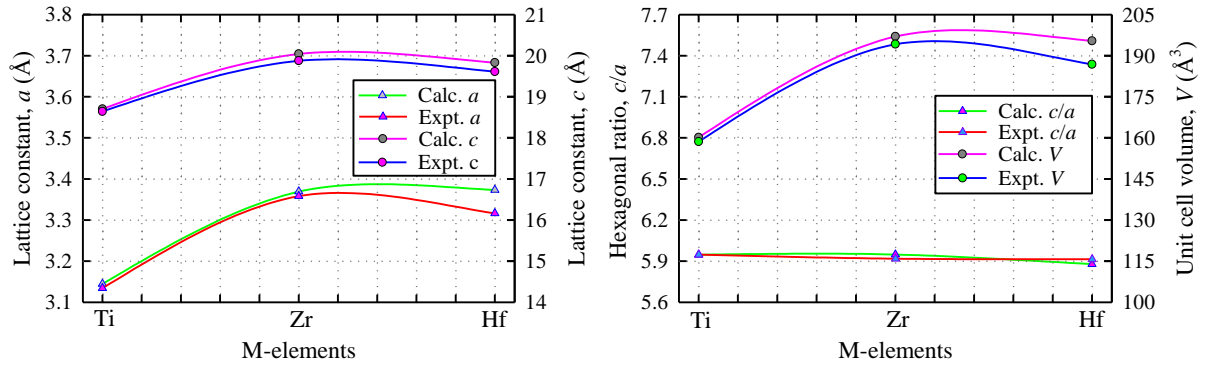


Fig. 1. Structural properties of M_3SnC_2 (M= Ti, Zr, Hf) as a function of M-element.

3.2 Mechanical properties

Mechanical properties are the physical properties that a material exhibits when a load is applied to it. Deep understanding of the mechanical properties is crucial for selecting a material to use in the appropriate field of application. Elastic constants are the main tools for evaluating the mechanical properties of solids. There are six different elastic constants C_{ij} namely C_{11} , C_{12} , C_{13} , C_{33} , C_{44} , and C_{66} for MAX phases due to their hexagonal crystal structure. Excepting $C_{66} [(C_{11} - C_{12})/2]$, all others are independent. The calculated elastic constants are listed in **Table 2** and shown in **Fig. 2**. The mechanical stability of hexagonal crystals depends on the conditions derived from the independent elastic constants: $C_{11} > 0$, $C_{33} > 0$, $C_{44} > 0$, $(C_{11} - C_{12}) > 0$, and $(C_{11} + C_{12})C_{33} > 2C_{13}^2$ [47]. The Sn-containing three 312 MAX phases Ti_3SnC_2 , Zr_3SnC_2 and Hf_3SnC_2 satisfy these conditions with their C_{ij} and establish their mechanical stabilities theoretically.

Table 2. Elastic properties of M_3SnC_2 (M = Ti, Zr, and Hf) MAX phases.

Phases	C_{11}	C_{33}	C_{44}	C_{66}	C_{12}	C_{13}	B	G	Y	B/G	ν	μ_M	Remarks
Ti_3SnC_2	321	304	115	110	100	79	162	114	276	1.42	0.215	1.41	This Calc.
	331	285	108	118	96	97	180	126	307	1.43	0.216	1.67	Calc. [8]
	346	313	123	127	92	84	169	124	300	1.36	0.205	1.37	Calc. [46]
Zr_3SnC_2	280	257	110	94	92	84	148	99	243	1.49	0.227	1.35	This Calc.
	297	268	95	103	90	87	154	98	244	1.57	0.237	1.62	Calc. [8]
Hf_3SnC_2	320	300	115	113	95	96	168	112	275	1.50	0.227	1.46	This Calc.
	326	300	107	116	96	97	170	110	272	1.55	0.233	1.59	Calc. [8]

The pure shear elastic constants C_{44} for the three Sn-containing 312 MAX phases are found to be lower than the unidirectional elastic constants C_{11} and C_{33} . This means that the shear deformation for the three phases is easier than linear compression along the crystallographic a - and c -axes following the order of M-elements: $Ti > Hf > Zr$. Again, the constant C_{11} is greater than C_{33} , indicating that the three crystals are more compressible along the c -axis compared to along the a -axis. It also implies that the atomic bonding between nearest atoms in the (001) planes is somewhat weaker than that in the (100) planes. Among the three MAX phases, the Zr_3SnC_2 is most compressible and Ti_3SnC_2 most incompressible along the c -axis. The difference of these two unidirectional elastic constants can quantify the elastic anisotropy in crystals. Regarding this, the Sn-containing three 312 MAX phases are elastically anisotropic.

The direction within the lattice is the main difference between the elastic constants C_{12} and C_{44} : the C_{12} governs the response to stress in the (110) plane and $\langle 100 \rangle$ direction, whereas the stress at the (010) plane in the $\langle 001 \rangle$ direction is affected by C_{44} . It is evident from **Table 2** that Zr_3SnC_2 is

deformed easily compared to other Sn-containing 312 phases. The combination of C_{12} and C_{13} leads to a functional stress along the crystallographic a -axis when a uniaxial strain exists in both the b - and c -axes. The low values of these constants imply that the M_3SnC_2 phases will accept shear deformation along the b - and c -axis, when an adequate stress is applied to the a -axis of the crystals.

We have also calculated the bulk elastic properties, namely bulk modulus, shear modulus, Young's modulus, etc. The bulk modulus B evaluates the resistance of solids under compression and can be related to the chemical bonding. With the lowest B value, Zr_3SnC_2 should be easily compressed and weak in chemical bonding compared to other two Sn-containing 312 MAX phases. The shear modulus G measures the materials' resistance to shape change. The Zr-based Zr_3SnC_2 has also lowest G value and as a result, its shape change should be easier than Ti- and Hf-based MAX phases considered here. The Young's modulus E reflects the stiffness of materials and has influence on the thermal shock resistance. A large E value makes a material stiffer and a low E value corresponds to a less-stiff material. It is evident from Table 2 that the Zr-based phase Zr_3SnC_2 is less stiff, and the Ti-based phase Ti_3SnC_2 is stiffer among the three MAX compounds studied here. The critical thermal shock resistance R varies inversely proportional to E [48]. A low E value corresponds to a high R value and better thermal shock resistance. A material will be selected as a thermal barrier coating (TBC) material if it has high thermal shock resistance. In the M_3SnC_2 system, the replacement of M-element with Zr causes a significant decrease in Young's modulus and as a result Zr_3SnC_2 should be a better TBC material than the other two MAX phases.

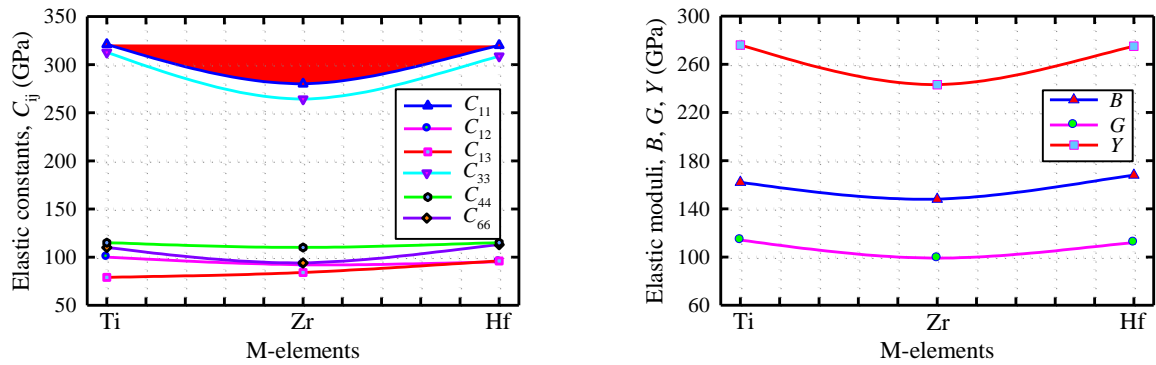


Fig. 2. Elastic constants and moduli of M_3SnC_2 (M= Ti, Zr, Hf) as a function of M-element.

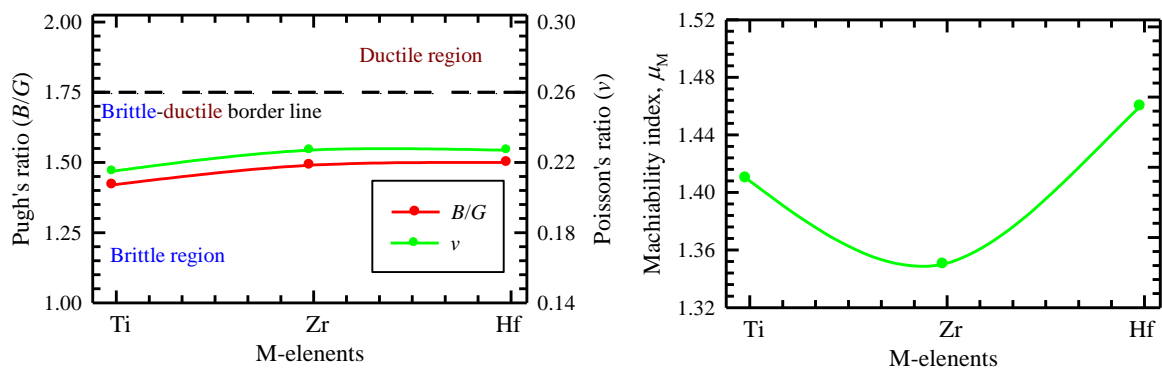


Fig. 3. Failure mode and Machinability indices of M_3SnC_2 (M= Ti, Zr, Hf) as a function of M-element.

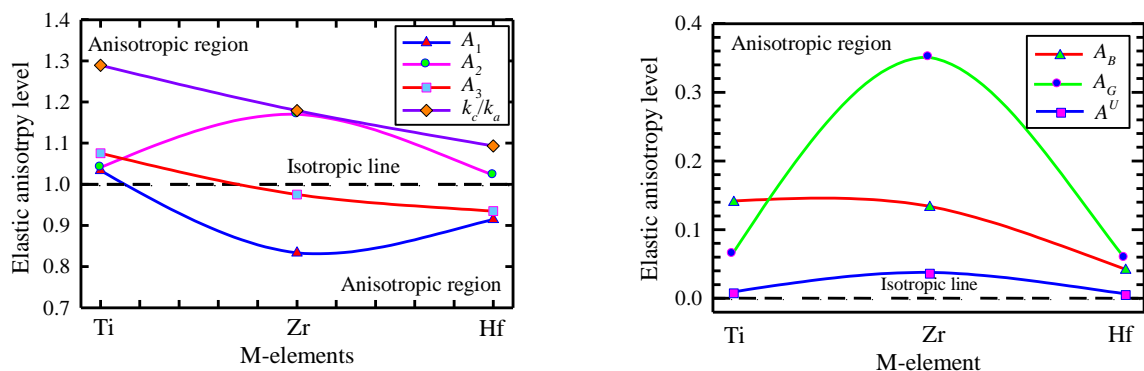


Fig. 4. Elastic anisotropy factors of M_3SnC_2 (M= Ti, Zr, Hf) as a function of M-element.

MAX phases are used in a wide range of industrial applications such as disk drive [4], Kiln furniture [4], etc. due to their good machinability, which is quantified with machinability index $\mu_M = B/C_{44}$. The calculated values of this parameter for the three Sn-containing 312 MAX phases are listed in **Table 2** and shown in **Fig. 3** as a function of M-element.

Using the bulk to shear modulus ratio (B/G), Pugh successfully predicted the brittle/ductile failure mode of solids [49]. According to Pugh's prediction, a material exhibits ductile nature when its B/G ratio exceeds a critical value of 1.75, or is brittle in nature below 1.75. Under this criterion, the studied three MAX phases should behave as brittle materials.

Poisson's ratio ν is used in engineering science for assessing the ductile/brittle failure mode of solids. A critical value of $\nu = 0.26$ can separate solids as ductile or brittle [50,51]. A solid, whose $\nu > 0.26$, behaves as a ductile material and that with $\nu < 0.26$ as a brittle one. Again, the studied three 312 MAX phases are identified as brittle materials under this factor. Poisson's ratio can also shed light on the nature of stabilizing force in solids [52]. The structure of a crystal will be stabilized with central force if its Poisson's ratio lies within 0.25-0.50. When the value of ν lies outside this range, the solids achieve structural stability due to non-central force. In this respect, the Sn-containing Ti_3SnC_2 , Zr_3SnC_2 and Hf_3SnC_2 maintain their structural stability under non-central force.

It is crucial to quantify the elastic anisotropy of crystals for many physical processes including development of plastic deformation in crystals, microscale cracking in ceramics, focusing of phonons in crystallites, etc. There are three shear anisotropy factors for hexagonal crystals due to their three independent shear elastic constants. The shear anisotropy factors associated with the shear planes $\{100\}$, $\{010\}$ and $\{001\}$ can be defined sequentially as [53]:

$$A_1 = \frac{(C_{11} + C_{12} + 2C_{33} - 4C_{13})}{6C_{44}}, \quad (1)$$

$$A_2 = \frac{2C_{44}}{C_{11} - C_{12}}, \quad (2)$$

$$A_3 = \frac{(C_{11} + C_{12} + 2C_{33} - 4C_{13})}{3(C_{11} - C_{12})} \quad (3)$$

The calculated shear anisotropy factors are listed in **Table 3** and shown in **Fig. 4**. The unit value of these indexes signifies the complete isotropic nature of crystals. Elastic anisotropy can be quantified with the deviation of these factors from unit value. The present values indicate that the Ti-based Ti_3SnC_2 is nearly isotropic and Zr-based Zr_3SnC_2 is rather anisotropic in view of shear stress.

Table 3. Calculated elastic anisotropy factors of M_3SnC_2 (M = Ti, Zr, and Hf) MAX phases.

Phases	A_1	A_2	A_3	k_c/k_a	A_B	A_G	A^U	Remarks
Ti_3SnC_2	1.0333	1.0407	1.0754	1.2892	0.1417	0.0648	0.0093	This Calc.
	0.8398	0.9191	0.8638	1.2394				Calc. [8]*
	0.9864	0.9398	0.9554	1.0305				Calc. [46]*
Zr_3SnC_2	0.8333	1.1702	0.9752	1.1792	0.1343	0.3512	0.0378	This Calc.
	1.0088	0.9179	0.9259	1.1768				Calc. [8]*
Hf_3SnC_2	0.9145	1.0222	0.9348	1.0931	0.0430	0.0590	0.0068	This Calc.
	0.9875	0.9304	0.9188	0.9956				Calc. [8]*

*Calculated with published data.

We have also calculated another important anisotropy factor defined as the ratio of linear compressibility coefficient along the c -axis to that along the a -axis: $k_c/k_a = (C_{11} + C_{12} - 2C_{13})/(C_{33} - C_{13})$. For isotropic crystals, this ratio is found to be unit value. Any value other than unity indicates

the degree of elastic anisotropy in axial compression. The obtained values signify that the axial compression response along the c -axis is greater than that along the a -axis for Ti_3SnC_2 and for Hf_3SnC_2 the linear compression along both axes is almost the same.

Percentage anisotropy in compressibility and shear are assumed to be more expedient measures of elastic anisotropy in polycrystalline solids. These two indices are expressed successively as follows [54]:

$$A_B = \frac{B_V - B_R}{B_V + B_R} \times 100\% \quad (4)$$

and

$$A_G = \frac{G_V - G_R}{G_V + G_R} \times 100\% \quad (5)$$

In these formulae, B and G are the bulk and shear moduli and their subscripts V and R stand for the Voigt and Reuss limits, respectively. For completely isotropic materials, A_B and A_G are found to be zero and values greater than zero indicate the increasing level of anisotropy associated with the crystals. A value of 100% for both A_B and A_G suggests the highest achievable anisotropy for a crystal. The listed values in Table 3 signify that the anisotropy in compression is slightly significant in Ti_3SnC_2 and anisotropy in shear is prominent in Zr_3SnC_2 .

The above-mentioned anisotropy factors lack universality in the sense of uniqueness and pay no attention to the contributions from the bulk part of the elastic stiffness tensor. To overcome these limitations, Shivakumar *et al.* [55] proposed a new index named universal elastic anisotropy. The new anisotropy factor is applicable to all types of crystals from cubic to triclinic. This factor is defined as:

$$A^U = 5 \frac{G_V}{G_R} + \frac{B_V}{B_R} - 6 \geq 0 \quad (6)$$

Like A_B and A_G factors, A^U also signifies the isotropic nature of crystals with $A^U = 0$ and quantifies the degree of anisotropy with a value greater than zero. Though the Sn-containing three 312 MAX phases, have low elastic anisotropy, the Zr-based Zr_3SnC_2 is 4 and 5.5 times more anisotropic compared to Ti and Hf-based Ti_3SnC_2 and Hf_3SnC_2 , respectively.

Melting and Debye temperatures

To determine the melting temperature of a compound, Fine *et al.* [56] developed an empirical formula:

$$T_m = 354 + 1.5(2C_{11} + C_{33}) \quad (7)$$

The estimated melting temperature is also listed in **Table 4** and shown in **Fig. 5**. It is observed that the melting temperature decreases drastically if Ti is replaced with Zr. While Ti is substituted by Hf it remains almost unchanged.

Anderson developed a sophisticated method for calculating the Debye temperature from elastic moduli with high precision [57]. This method is valid for all crystal classes and it requires no intensive computing. According to this method, the Debye temperature of a solid is directly proportional to the average sound velocity, with which sound waves travel through the material. For polycrystalline materials, where the transverse and longitudinal sound velocities remain invariant with direction, the average sound velocity can be expressed as:

$$v_m = \left[\frac{1}{3} \left(\frac{1}{v_l^3} + \frac{2}{v_t^3} \right) \right]^{-1/3} \quad (8)$$

The longitudinal sound velocity, v_l and transverse sound velocity v_t are computed from the bulk and shear moduli B , G and mass density ρ of the material as follows:

$$v_t = \left[\frac{G}{\rho} \right]^{1/2} \quad \text{and} \quad v_l = \left[\frac{(3B + 4G)}{3\rho} \right]^{1/2} \quad (9)$$

The Debye temperature, θ_D is then easily computed by the simple equation:

$$\theta_D = \frac{h}{k_B} \left[\frac{3nN_A \rho}{4\pi M} \right]^{1/3} v_m \quad (10)$$

The calculated sound wave velocities and Debye temperature are listed in Table 4 and presented in Fig. 5. A gradual decrease in sound velocities is observed when the M-element moves from Ti to Hf. The Debye temperature decreases significantly when the Ti-atom is replaced with Zr-atom. The decrease in Debye temperature will be one-third if the Zr-atom is then substituted by the Hf-atom.

Table 4. Calculated density (ρ in gm/cm³), longitudinal, transverse and average sound velocities (v_l , v_t , v_m in km/s), Debye temperature (θ_D in K) and melting temperature of M₃SnC₂ (M = Ti, Zr, and Hf) MAX phases.

Phases	ρ	v_t	v_l	v_m	θ_D	T_m	Remarks
Ti ₃ SnC ₂	5.9354	4.3826	7.2734	5.6006	703	1764	This Calc.
	5.9059	4.6189	7.6762	5.9050	740	1766	Calc. [8]*
	6.1266	4.4988	7.3872	5.7303	727	1853	Calc. [46]*
Zr ₃ SnC ₂	7.0192	3.7556	6.3159	4.8184	480	1571	This Calc.
	6.9452	3.7564	6.4022	4.8383	531	1638	Calc. [8]*
Hf ₃ SnC ₂	11.5259	3.1172	5.2471	3.4517	405	1755	This Calc.
	11.8286	3.0495	5.1741	3.9227	465	1773	Calc. [8]*

*Calculated with published data.

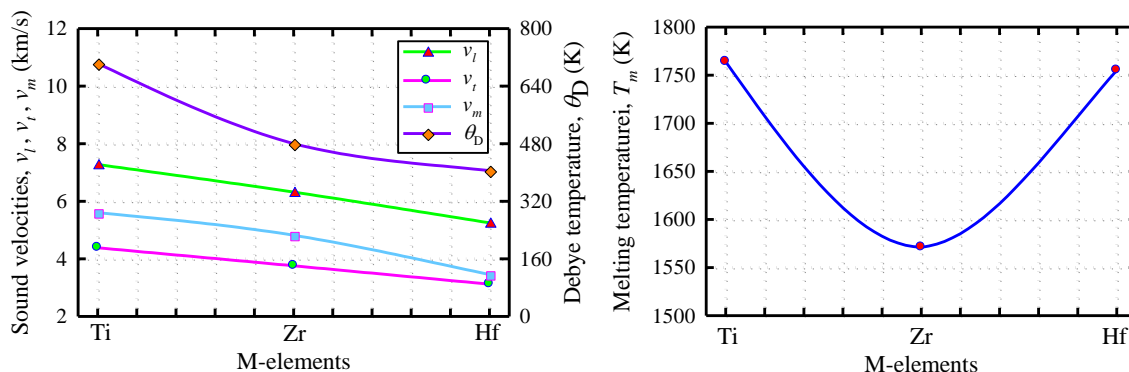


Fig. 5. Melting and Debye temperatures with sound wave velocities as a function of M-element.

3.3. Electronic structures

The electronic band structures for the three Sn-based 312 MAX phases calculated along the high-symmetry directions are shown in **Fig. 6**. The Fermi levels are set at zero of the energy scale defined with $E - E_F$. The Fermi surfaces lie below the valence band maximum near the Γ -point. A number of valence bands go across the Fermi level and overlap with the conduction bands. Consequently, no band gap appears at the Fermi level and the compounds Ti₃SnC₂, Zr₃SnC₂ and Hf₃SnC₂ should exhibit metallic conductivity. The Γ -points, where the maximum valence bands accumulate, shift away from the Fermi surface as the M-element moves from Ti to Hf across the periodic table. The width of the conduction bands increases as the M-element goes down from top of the group in the periodic table, indicating the increasing level of electrical conductivity. As the broadening of the conduction band indicates strengthen electron delocalization and the delocalized electrons are responsible for the electrical conductivity [**-**]. In the Ti₃SnC₂, Zr₃SnC₂ and Hf₃SnC₂ phases, 2.2, 4.0 and 4.2 eV above the Fermi level are found to be involved in electrical conduction. M d-electrons with covalent bond to C have the dominant contribution in the conductivity [**-**]. Other features and shapes of the band profiles are almost similar in the three MAX phase carbides.

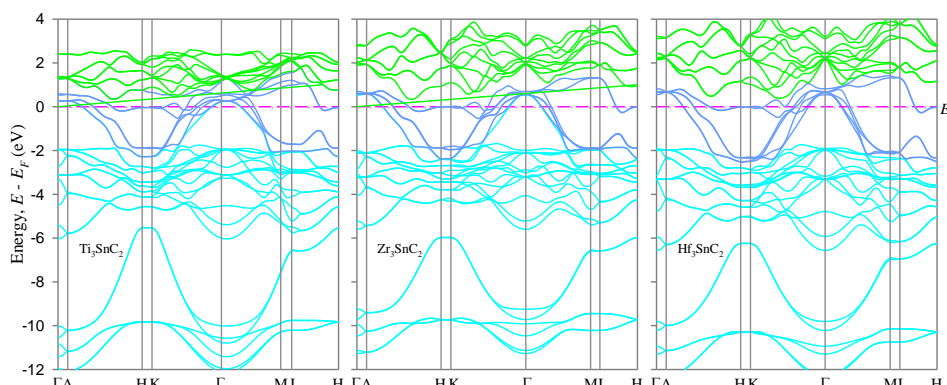


Fig. 6. Band structures of M_3SnC_2 ($M = Ti, Zr, \text{ and } Hf$) MAX phases.

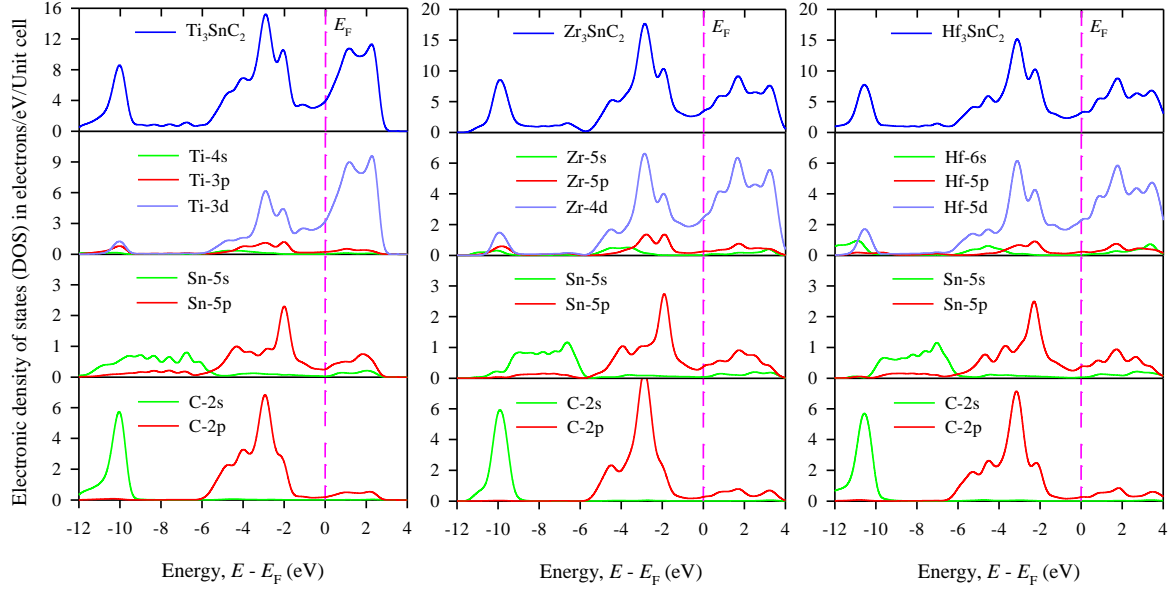


Fig. 7. Electronic density of states of M_3SnC_2 ($M = Ti, Zr, \text{ and } Hf$) MAX phases.

The calculated total and partial density of states (DOS) for the three Sn-containing 312 MAX phases are shown in Fig. 7. In the DOS, the peak structures and their relative heights are almost the same. The main differences are found in the structure of conduction bands as well as in the shape of the lowest valence bands due to the Sn 5s electrons. The presence of a pseudogap at the left of the Fermi level E_F in the DOS is a sign of the structural stability of these compounds. The finite value of DOS at E_F indicates the metallic nature of M_3SnC_2 . As a trend of MAX phases [23,28,31,33,58,59], the d-orbitals of transition metals (here Ti 3d, Zr 4d and Hf 5d) mainly contribute to the DOS at E_F and no contribution comes from carbon. The obtained DOS at E_F are found to be 3.925, 3.448 and 3.217 states per eV per unit cell for Ti_3SnC_2 , Zr_3SnC_2 and Hf_3SnC_2 , respectively, indicating a gradual decrease in DOS at E_F following the order of M-element in the periodic table.

The lower valence bands centered around -10 eV arise in the three Sn-containing MAX phases due to hybridization between C s electrons and transition metal M d electrons, which lead to strong covalent M-C bonds. A low flat-type valence band exists between the lower and higher valence bands due to s-orbital electrons of the Sn-atoms. The highest peak in the higher valence band originates as a result of strong hybridization of C p and M d orbitals, which also indicates another M-C covalent bond. The M-C bond mentioned early will be strongest as it corresponds to the lowest valence states situated at a deeper energy region. The lowest peak in the higher valence band is mainly composed of Sn p and M d electrons, which indicates weaker M-Sn bonds due to proximity to the Fermi level of the peak. It is the common feature of the MAX phases [23,28]. On the whole, the bonding nature in the three Sn-containing MAX phases in the 312 sub-family can be described as a combination of metallic, covalent, and, due to the difference in electronegativity between the comprising elements, ionic contributions.

Mulliken population analysis

Mulliken population analysis performed with LCAO basis sets provides a natural way to quantify the atomic charge, effective valence, bond population and charge transfer [60,61]. The charge assigned with a particular atom A can be calculated by:

$$Q(A) = \sum_k w_k \sum_{\mu}^{on A} \sum_{\nu} P_{\mu\nu}(k) S_{\mu\nu}(k)$$

and the overlap population between two atomic species A and B, is

$$P(AB) = \sum_k w_k \sum_{\mu}^{on A} \sum_{\nu}^{on B} 2P_{\mu\nu}(k) S_{\mu\nu}(k)$$

where $P_{\mu\nu}$ is the density matrix element and $S_{\mu\nu}$ is the overlap matrix. The Mulliken atomic charge on the anion species initiates to evaluate the effective valence from the formal ionic charge. The difference of these two characteristic charges evaluates the effective valence of an atomic species. The effective valence quantifies the strength of a chemical bond identifying with covalency or ionicity. A zero-value effective valence is observed to be assigned with a bond of type purely ionic and a non-zero effective valence leads to form a bond of covalent nature. The increasing level of covalency of a chemical bond can be evaluated with the value of a positive effective valence. The effective valence calculated for the Sn-based three 312 MAX phases is presented in **Table 5**. The data presented in **Table 5** indicate the dominant covalency in chemical bonding between constituent atoms in Ti_3SnC_2 , Zr_3SnC_2 and Hf_3SnC_2 . The charge transfer from one atom to another can be estimated from the analysis of the atomic populations. In Ti_3SnC_2 the charge transfer from Ti to C and Sn is 0.72 and 0.11e, respectively. Similarly, 0.79 and 0.09e charges are transferred from Ti atom to C and Sn atoms, respectively. Conversely, in Hf_3SnC_2 , instead of charge receiving Sn atom takes part in charge transferring. The carbon atom receives 0.87e charge from Sn and Ti atoms. The charge transfer between to atoms indicates their ionic bonding.

Table 5. Mulliken atomic populations, Mulliken charge and effective valence of M_3SnC_2 .

Compounds	Mulliken atomic populations					Total	Charge / e	Effective valence / e
	Species	s	p	d				
Ti_3SnC_2	C	1.48	3.24	0.00		4.72	-0.72	----
	Sn	1.53	2.57	0.00		4.11	-0.11	3.89
	Ti1	2.13	6.60	2.61		11.33	-0.67	3.33
	Ti2	2.19	6.67	2.70		11.56	-0.44	3.56
Zr_3SnC_2	C	1.50	3.29	0.00		4.79	-0.79	----
	Sn	1.53	2.56	0.00		4.09	-0.09	3.91
	Zr1	2.17	6.46	2.60		11.23	-0.77	3.23
	Zr2	2.26	6.56	2.74		11.55	-0.45	3.55
Hf_3SnC_2	C	1.55	3.32	0.00		4.87	-0.87	----
	Sn	1.05	2.65	0.00		3.69	-0.31	3.69
	Hf1	0.41	0.05	2.74		3.21	-0.79	3.21
	Hf2	0.47	0.37	2.83		3.67	-0.33	3.67

The bond overlap population plays an important role to predict the bonding nature in crystalline solids. Weak interactions of electronic populations between two atoms give rise to an overlap population of zero value. As bond population approaches a zero value, the ionic nature of the chemical bonding increases. Conversely, a higher positive population indicates higher covalent nature in the chemical bonding. A negative value of overlap population is responsible for the antibonding states in the chemical bonding. The bond overlap population for the studied MAX phases is listed in Table 6.

The covalency of both M-C bonds is found to be increased as the M-atom moves from Ti to Hf via Zr. The antibonding states due to M-Sn bonding weaken as Ti is replaced with Zr and alter into bonding state when M-atom is Hf. The M-M bonding gives rise to the antibonding states in the three Sn-containing 312 MAX phases.

Table 6. Mulliken bond number n^μ , bond length d^μ , and bond overlap population P^μ of μ -type bond of M_3SnC_2 .

Ti_3SnC_2				Zr_3SnC_2				Hf_3SnC_2			
Bond	n^μ	$d^\mu/\text{\AA}$	P^μ	Bond	n^μ	$d^\mu/\text{\AA}$	P^μ	Bond	n^μ	$d^\mu/\text{\AA}$	P^μ
Ti1-C	4	2.0954	-1.21	Zr1-C	4	2.2697	-1.24	Hf1-C	4	2.2811	-1.57
Ti2-C	4	2.2209	-0.87	Zr2-C	4	2.3973	-0.88	Hf2-C	4	2.3884	-1.07
Ti1-Sn	4	2.9701	-0.66	Zr1-Sn	4	3.1205	-0.22	Hf1-Sn	4	3.0807	-0.03
Ti1-Ti2	4	2.9500	-0.50	Zr1-Zr2	4	3.2237	-0.27	Hf1-Hf2	4	3.2248	-0.37

3.4. Theoretical hardness

Hardness is one of the most important mechanical properties of solid materials, depending on which a material is selected for engineering usages. Theoretical Vickers hardness calculation has an increasing interest in recent time after reformulation of the Gao [62] formalism for partially metallic compounds [63]. The bond hardness due to this reformulation is as follows:

$$H_v^\mu = 740 \left(P^\mu - P^{\mu'} \right) (v_b^\mu)^{-5/3} \quad (13)$$

where the Mulliken population for a bond of type μ is denoted by P^μ , $P^{\mu'}$ refers to the metallic population, and v_b^μ represents the volume of a μ -type bond. Again, the metallic population is defined as the number of free electrons confined in a cell per unit volume and can be calculated as:

$$P^{\mu'} = (1/V)n_{free} = (1/V) \int_{E_p}^{E_F} N(E)dE \quad (14)$$

where, E_p and E_F are the energy at the pseudogap and Fermi level, respectively. The bond volume of a μ -type bond v_b^μ can be determined from the bond length d^μ of type μ and the number of v-type bonds N_b^v per unit volume using the equation:

$$v_b^\mu = (d^\mu)^3 / \sum_v [(d^\mu)^3 N_b^v] \quad (15)$$

The hardness of a complex multiband crystal can be determined from the geometric average of all bond hardness values as follows [64,65]:

$$H_v = [\prod (H_v^\mu)^{n^\mu}]^{1/\sum n^\mu} \quad (16)$$

where n^μ refers to the number of μ -type bonds of a multiband crystal. The calculated Vickers hardness and relevant parameters are listed in Table 7.

Table 7. Calculated Vickers hardness H_v of M_3SnC_2 (M = Ti, Zr, Hf) MAX phases with the relevant quantities such as metallic population $P^{\mu'}$, bond volume v_b^μ and bond hardness H_v^μ .

Phases	Bond	n^μ	$d^\mu/\text{\AA}$	P^μ	$P^{\mu'}$	$v_b^\mu / \text{\AA}^3$	H_v^μ / GPa	H_v / GPa
Ti_3SnC_2	Ti1-C	4	2.0954	1.21	0.01285	18.28	6.98	5.1
	Ti2-C	4	2.2209	0.87	0.01285	21.77	3.74	
Zr_3SnC_2	Zr1-C	4	2.2697	1.24	0.00935	22.61	5.04	4.2
	Zr2-C	4	2.3973	0.88	0.00935	26.64	3.56	
Hf_3SnC_2	Hf1-C	4	2.2811	1.57	0.01663	22.74	6.30	4.7
	Hf2-C	4	2.3884	1.07	0.01663	25.87	3.44	

The obtained values for Vickers hardness of Ti_3SnC_2 , Zr_3SnC_2 and Hf_3SnC_2 are 5.1, 4.2 and 4.7 GPa, respectively. These values lie within the range 2-8 GPa for MAX phases [7,22,58,66], indicating the reliability of the present calculations as well as signifying that the three studied compounds are likely to be soft and easily machinable. The rank of machinability for these compounds should be $Zr_3SnC_2 > Hf_3SnC_2 > Ti_3SnC_2$.

3.5 Charge density maps and Fermi surfaces

To understand the chemical bonding in the three Sn-containing 312 MAX phases, the contour maps of electron charge density are investigated and presented in Fig. 8. The contour maps of Ti_3SnC_2 and Zr_3SnC_2 are almost identical, indicating the similar charge distribution and chemical bonding in the two nanolaminates. In these two compounds, the charge density distributions around M and Sn atoms are fairly spherical and around the C atom, it is distorted towards M atoms, indicating the strong M-C (Ti-C and Zr-C) covalent bonding. The charge distribution around the Hf atom in Hf_3SnC_2 is also spherical, but it indicates low density and encompasses a small area. The reason may be its smaller atomic populations compared to those of Ti and Zr (see Table 5). The charge distribution around C atoms in Hf_3SnC_2 is nearly spherical with a noticeable deformation in the direction of the Hf atoms, which also indicates strong Hf-C covalent bonding. In the three studied MAX phases, the charge distribution of C towards Sn is almost spherical, indicating the ionic nature of the Sn-C bonding.

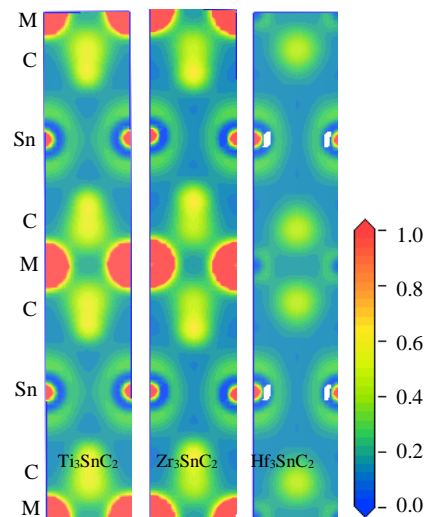


Fig. 8. Calculated charge density maps of M_3SnC_2 ($\text{M} = \text{Ti}, \text{Zr}, \text{Hf}$) MAX phases.

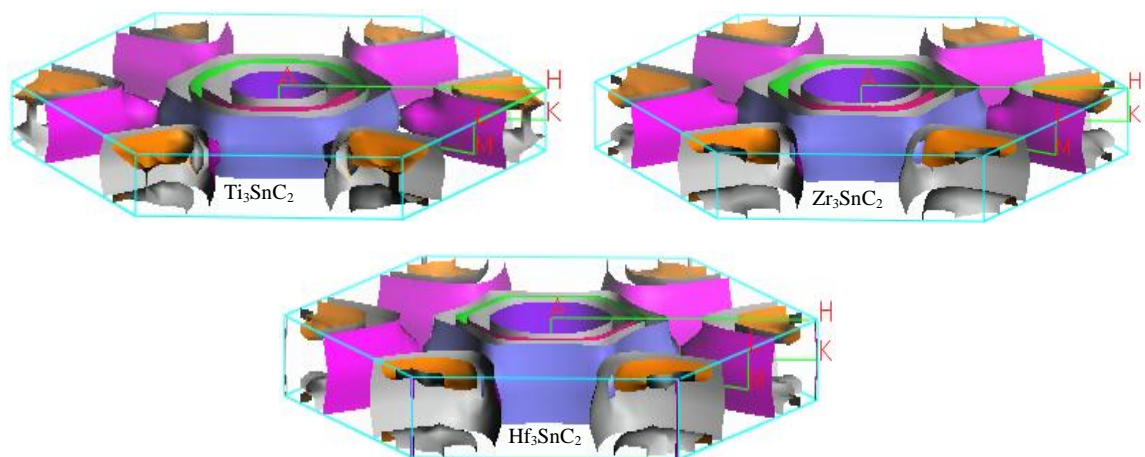


Fig. 9. Fermi surfaces of M_3SnC_2 ($\text{M} = \text{Ti}, \text{Zr}, \text{Hf}$) MAX phases.

The Fermi surface is a conceptual geometrical demonstration of all the accessible electronic states in a material, which leads to characterize a material with its electrical, thermal and magnetic properties. With the knowledge of Fermi surface one can predict the materials' electrical properties and aspire to develop materials with preferred functionality. The calculated Fermi surfaces of the three Sn-

containing 312 MAX phases are shown in Fig. 9. The Fermi surface topologies of the three 312 MAX phases are almost similar and comparable with those of their 211 MAX phase counterparts [67]. These topologies consist of different sheets. Four electron-like sheets are seen to be centered along the Γ -A direction. The first sheet is purely cylindrical and the other three sheets are prismatic-like with hexagonal cross sections. Two hole-like sheets with complex topology appear at the corners of the Brillouin zone around the H-K directions.

3.6 Defect processes

In essence the point defect processes can impact properties such as the radiation performance of materials. This will depend on the propensity of the material to form and accommodate point defects, as a high content of defects may lead to the destabilization of the system and even microcracking [68,69]. It has been determined that displacive radiation can lead to an athermal concentration of Frenkel pairs. In essence the radiation tolerance of a material can depend upon its resistance to form high populations of Frenkel (and antisite) defects and therefore high defect energies indicate radiation tolerance [70]. Table 8 reports the calculated defect reaction energies (in Kröger-Vink notation: *i.e.*, V_A and A_i will denote a vacant A site and an A interstitial defect respectively) and the corresponding defect for the Ti_3SnC_2 MAX phases ($M = Ti, Zr, Hf$), whereas Table 9 shows the corresponding lowest energy interstitial sites.

Table 8. The calculated defect reaction energies (in eV, for relations 1-18) for the M_3SnC_2 MAX phases ($M = Ti, Zr, Hf$).

Reaction	Ti_3SnC_2	Zr_3SnC_2	Hf_3SnC_2
1) $M_M \rightarrow V_M + M_i$	9.40	8.74	9.20
2) $Sn_{Sn} \rightarrow V_{Sn} + Sn_i$	9.41	6.48	7.29
3) $C_C \rightarrow V_C + C_i$	5.50	4.97	5.31
4) $M_M + Sn_{Sn} \rightarrow M_{Sn} + Sn_M$	5.38	5.15	5.21
5) $M_M + C_C \rightarrow M_C + C_M$	12.13	15.92	15.10
6) $Sn_{Sn} + C_C \rightarrow Sn_C + C_{Sn}$	10.18	10.09	10.63
7) $Sn_i + V_M \rightarrow Sn_M$	-7.36	-4.44	-4.86
8) $C_i + V_M \rightarrow C_M$	-1.75	-0.58	-0.13
9) $M_i + V_{Sn} \rightarrow M_{Sn}$	-6.07	-5.63	-6.42
10) $C_i + V_{Sn} \rightarrow C_{Sn}$	-0.07	0.31	0.12
11) $M_i + V_C \rightarrow M_{iC}$	-1.02	1.79	0.72
12) $Sn_i + V_C \rightarrow Sn_C$	-4.65	-1.67	-2.10
13) $M_i + Sn_{Sn} \rightarrow M_{Sn} + Sn_i$	3.34	0.85	0.88
14) $M_i + C_C \rightarrow M_C + C_i$	4.48	6.76	6.04
15) $Sn_i + M_M \rightarrow Sn_M + M_i$	2.05	4.30	4.33
16) $Sn_i + C_C \rightarrow Sn_C + C_i$	0.85	3.30	3.22
17) $C_i + M_M \rightarrow C_M + M_i$	7.65	8.16	9.07
18) $C_i + Sn_{Sn} \rightarrow C_{Sn} + Sn_i$	9.34	6.79	7.41

Table 9. The lowest energy interstitial sites for the M_3SnC_2 MAX phases ($M = Ti, Zr, Hf$).

Phases	M_i	Sn_i	C_i
Ti_3SnC_2	1/3, 2/3, 0.698	0.520, 0.488, 0.295	1/3, 2/3, 0.652

Zr ₃ SnC ₂	0.735, 0.689, 1/4	-0.084, 0.689, 1/4	1/3, 2/3, 1/4
Hf ₃ SnC ₂	0.771, 0.673, 1/4	2/3, 1/3, 1/4	1/3, 2/3, 1/4

Considering the intrinsic defect processes investigated here (relations 1-6 in Table 8) it can be inferred that Ti₃SnC₂ will be more radiation tolerant than Zr₃SnC₂ and Hf₃SnC₂. This is due to the lowest energy intrinsic disorder mechanism (5.38 eV, relation 4 in Table 8) in Ti₃SnC₂ being higher in energy compared to the lowest energy intrinsic disorder mechanisms in Zr₃SnC₂ and Hf₃SnC₂ (4.97 eV and 5.21 eV respectively, Table 8). Additionally, all the Frenkel energies of Ti₃SnC₂ are higher as compared to Zr₃SnC₂ and Hf₃SnC₂ (relations 1-3, Table 8). Therefore, there will be a lower concentration of antisite and Frenkel defects in Ti₃SnC₂ as compared to Zr₃SnC₂ and Hf₃SnC₂. Focusing on Ti₃SnC₂, given that relations 3 and 4 are the most favourable it is expected that there will be a higher concentration of C_i, V_C, Ti_{Sn} and Sn_{Ti} defects when the material will be irradiated. The other intrinsic defect processes (relations 1,2,5,6 of Table 8) are far higher in energy and never of importance. A trend that was identified in all Sn-MAX phases considered is that interstitial defects readily recombine with vacancies to form antisite defects (relations 7-9, 12 of Table 8), whereas the interactions of interstitials with lattice atoms to produce antisites is always energetically unfavourable (relations 13-18 of Table 8). It should be stressed that although defect reactions can provide important information on the radiation tolerance of MAX phases, they should be verified by experiments and/or theoretical calculations of diffusion barriers and cascade processes.

4. Conclusions

1. First-principles calculations were performed for investigation of intrinsic defect process and structural, elastic, and electronic properties of recently synthesized Sn-containing M₃SnC₂ (M = Ti, Zr, Hf) MAX phases.
2. The calculated lattice constants agree well with the experimental values. The lattice constant *a* is observed to increase as the M-element moves from Ti to Hf in the periodic table.
3. The computed single crystal elastic constants verify the mechanical stability of these compounds. The calculations show that the Hf-based Hf₃SnC₂ is nearly isotropic elastically.
4. The Debye temperatures are found to be dependent on M-element and decrease as the M-element moves from Ti to Hf. The machinability of these compounds should follow the order Zr₃SnC₂ > Hf₃SnC₂ > Ti₃SnC₂.
5. The covalency of M-C bonds is found to be increased as M-atoms moves from Ti to Hf via Zr. The Fermi surface topologies of Ti₃SnC₂, Zr₃SnC₂ and Hf₃SnC₂ are similar and comparable with those of 211 MAX phases' counterparts. Ti₃SnC₂ is the most radiation-tolerant Sn-MAX phase based on the defect reaction energies.

Acknowledgements

S-RGC, AC, and MEF are grateful for funding from the Lloyd's Register Foundation, a charitable foundation helping protect life and property by supporting engineering-related education, public engagement, and the application of research

References

- [1] M. W. Barsoum and T. El-Raghy, J. Am. Ceram. Soc. 79 (1996) 1953.
- [2] H. Kudielka and H. Rohde, Z. Kristallogr. 114(1-6) (1960) 447-456.

- [3] P. Eklund, J.-P. Palmquist, J. Höwing, D. H. Trinh, T. El-Raghy, H. Högberg, I. Hultman, *Acta Mater.* 55 (2007) 4723.
- [4] M. W. Barsoum, *Prog. Solid State Chem.* 28 (2000) 201-281.
- [5] D. Horlait, S. Grasso, A. Chroneos, and W. E. Lee, *Mater Res. Lett.* 4, 137 (2016).
- [6] Z. M. Sun, *Int. Mater. Reviews* 56 (2011) 143-166.
- [7] M. A. Hadi, *Comp. Mater. Sci.* 117 (2016) 422-427.
- [8] S. Aryal, R. Sakidja, M. W. Barsoum, and W.-Y. Ching, *Phys. Stat. Solidi B* 251 (2014) 1480-1497.
- [9] T. Lapauw, K. Lambrinou, T. Cabioc'h, J. Halim, J. Lu, A. Pesach, O. Rivin, O. Ozeri, E.N. Caspi, L. Hultman, P. Eklund, J. Rosén, M.W. Barsoum, J. Vleugels, *J. Euro. Ceram. Soc.* 36 (2016) 1847–1853.
- [10] T. Lapauw, B. Tunca, T. Cabioc'h, J. Lu, P. O. Å. Persson, K. Lambrinou, and J. Vleugels, *Inorg. Chem.* 55 (2016) 10922-10927.
- [11] T. Lapauw, J. Halim, J. Lu, T. Cabioc'h, L. Hultman, M.W. Barsoum, K. Lambrinou, J. Vleugels, *J. Euro. Ceram. Soc.* 36 (2016) 943–947.
- [12] T. Lapauw, B. Tunca, T. Cabioc'h, J. Vleugels and K. Lambrinou, *J. Euro. Ceram. Soc.* 37 (2017) 4539-4545.
- [13] S. Dubois, T. Cabioc'h, P. Chartier, V. Gauthier, and M. Jaouen, *J. Am. Ceram. Soc.* 90 (2007) 2642-2644.
- [**] Z. Yan, L. Chen, M. Yoon and S. Kumar, *Nanoscale* 8 (2016) 4037-4046
- [14] P. Hohenberg and W. Kohn, *Phys. Rev.* 136 (1964) B864.
- [15] W. Kohn and L.J. Sham, *Phys. Rev.* 140 (1965) A1133.
- [16] S. J. Clark, M. D. Segall, C. J. Pickard, P. J. Hasnip, M. I. J. Probert, K. Refson, and M. C. Payne, *Z. Kristallogr.* 220 (2005) 567.
- [17] D. Vanderbilt, *Phys. Rev. B* 41 (1990) 7892.
- [18] J.P. Perdew, K. Burke, and M. Ernzerhof, *Phys. Rev. Lett.* 77 (1996) 3865.
- [19] T.H. Fischer and J. Almlof, *J. Phys. Chem.* 96 (1992) 9768.
- [20] H. J. Monkhorst and J. D. Pack, *Phys. Rev. B* 13 (1976) 5188.
- [21] F. D. Murnaghan, *Finite Deformation of an Elastic Solid* (Wiley, New York, 1951).
- [22] M. Roknuzzaman, M.A. Hadi, M.A. Ali, M.M. Hossain, N. Jahan, M.M. Uddin, J.A. Alarco, K. Ostrikov, *J. Alloys Comp.* 727 (2017) 616-626.
- [23] M.A. Hadi, S.H. Naqib, S.-R.G. Christopoulos, A. Chroneos, A.K.M.A. Islam, *J. Alloys Compd.* 724 (2017) 1167.
- [24] Mirza H.K. Rubel, M.A. Hadi, M.M. Rahaman, M.S. Ali, M. Aftabuzzaman, R. Parvin, A.K.M.A. Islam, N. Kumada, *Comp. Mater. Sci.* 138 (2017) 160.
- [25] M.A. Hadi, M. Roknuzzaman, A. Chroneos, S.H. Naqib, A.K.M.A. Islam, R.V. Vovk, K. Ostrikov, *Comp. Mater. Sci.* 137 (2017) 318.

- [26] M. A. Ali, M. A. Hadi, M. M. Hossain, S. H. Naqib, and A. K. M. A. Islam, *Phys. Status Solidi B* 254 (2017)1700010.
- [27] M A Hadi, M S Ali, S H Naqib, and A K M A Islam, *Chin. Phys. B* 26 (2017) 037103.
- [28] M. A. Hadi and M. S. Ali, *Chin. Phys. B* 25 (2016) 107100.
- [29] M. A. Hadi, M. T. Nasir, M. Roknuzzaman, M. A. Rayhan, S. H. Naqib, and A. K. M. A. Islam, *Phys. Status Solidi B* 253 (2016) 2020.
- [30] M. A. Alam, M. A. Hadi, M. T. Nasir, M. Roknuzzaman, F. Parvin, M. A. K. Zilani, A. K. M. A. Islam, S. H. Naqib, *J. Supercond. Nov. Magn.* 29 (2016) 2503.
- [31] M. Roknuzzaman, M.A. Hadi, M.J. Abden, M.T. Nasir, A.K.M.A. Islam, M.S. Ali, K. Ostrikov, S.H. Naqib, *Comp. Mater. Sci.* 113 (2016) 148.
- [32] M. A. Hadi, M. A. Alam, M. Roknuzzaman, M. T. Nasir, A. K. M. A. Islam, and S. H. Naqib, *Chin. Phys. B* 24 (2015) 117401.
- [33] M. T. Nasir, M. A. Hadi, S. H. Naqib and F. Parvin, A. K. M. A. Islam, M. Roknuzzaman and M. S. Ali, *Int. J. Mod. Phys. B* 28 (2014) 1550022.
- [34] W. Voigt, *Lehrbuch der Kristallphysik*, (Taubner, Leipzig, 1928).
- [35] A. Reuss, *Z. Angew. Math. Mech.* 9 (1929) 55.
- [36] R. Hill, *Proc. Phys. Soc. London* 65 (1952) 350.
- [37] D. Sanchez-Portal, E. Artacho, and J. M. Soler, *Soid State Commun.* **95**, 685 (1995).
- [38] R. S. Mulliken, *J. Chem. Phys.* **23**, 1833 (1955).
- [39] D. Horlait, S. Middleburgh, A. Chroneos, and W. E. Lee, *Sci. Rep.* **6**, 18829 (2016).
- [40] E. Zapata-Solvas, S.-R. G. Christopoulos, N. Ni, D. C. Parfitt, D. Horlait, M. E. Fitzpatrick, A. Chroneos, and W. E. Lee, *J. Am. Ceram. Soc.* 100 (2017) 1377.
- [41] E. Zapata-Solvas, M. A. Hadi, D. Horlait, D. C. Parfitt, A. Thibaud, A. Chroneos, and W. E. Lee, *J. Am. Ceram. Soc.* 100, 3393 (2017).
- [42] L. Farber, I. Levin, and M. W. Barsoum, *Philos. Mag. Lett.* 79 (1999) 163–70.
- [43] R. Yu, Q. Zhan, L. L. He, Y. C. Zhou, and H. Q. Ye, *J. Mater. Res.* 17 (2002) 948–950.
- [44] Z. W. Wang, C. S. Zha, and M. W. Barsoum, *Appl. Phys. Lett.*, 85 (2004) 3453–3455.
- [45] J. Y. Wang and Y. C. Zhou, *Phys. Rev. B*, 69 (2004) 144108.
- [46] X. He, Y. Bai, Y. Chen, C. Zhu, M. Li, and M. W. Barsoum, *J. Am. Ceram. Soc.* 94 (2011) 3907–3914.
- [47] M. Born, *On the stability of crystal lattices. I*, *Mathematical Proceedings of the Cambridge Philosophical Society*, Cambridge University Press, 1940, pp. 160.
- [48] X. Wang, H. Xiang, X. Sum, J. Liu, F. Hou, Y. Zhou, *J. Mater. Sci. Technol.* 31 (2015) 369.
- [49] S.F. Pugh, *Philos. Mag.* 45 (1954) 823-843.
- [50] I. N. Frantsevich, F. F. Voronov, and S. A. Bokuta, *Elastic Constants and Elastic Moduli of Metals and Insulators Handbook* (Naukova Dumka, Kiev, 1983), pp. 60–180.

- [51] G. Vaitheeswaran, V. Kanchana, A. Svane, and A. Delin, *J. Phys.: Condens. Matter* **19**, 326214 (2007).
- [52] O. L. Anderson and H. H. Demarest Jr., *J. Geophys. Res.* **76**, 1349 (1971).
- [53] H. M. Ledbetter, *J. Phys. Chem. Ref. Data* **6** (1977) 1181.
- [54] D. H. Chung and W. R. Buessem, in *Anisotropy in Single Crystal Refractory Compound*, edited by F. W. Vahldiek and S. A. Mersol, Vol. 2 (Plenum, New York, 1968), p. 217.
- [55] I. Shivakumar, Ranganathan and M. Ostoja-Starzewski, *Phys. Rev. Lett.*, **101** (2008) 055504.
- [56] M. E. Fine, L. D. Brown, and H. L. Mercus, *Scripta Metallurgia* **18** (1984) 951-956.
- [57] O.L. Anderson, *J. Phys. Chem. Solids* **24** (1963) 909.
- [**] P.-H. Huang and C.-M. Lu, *The Scientific World Journal*, Volume 2014 (2014), Article ID 863404.
- [**] B. A. Averill and P. Eldredge, *Principles of General Chemistry* (v. 1.0), ebook link: <https://2012books.lardbucket.org/books/principles-of-general-chemistry-v1.0/s16-06-bonding-in-metals-and-semicond.html>.
- [**] [35]G. Hug and E. Fries, *Phys. Rev. B* **65** (2002) 113104.
- [58] M. A. Hadi, M. Roknuzzaman, F. Parvin, S. H. Naqib, A. K. M. A. Islam and M. Aftabuzzaman, *J. Sci. Res.* **6** (2014) 11-27.
- [59] M. A. Hadi, R. V. Vovk, and A. Chronos, *J. Mater. Sci.: Mater. Electron* **27** (2016)11925–11933.
- [60] D. Sanchez-Portal, E. Artacho, and J. M. Soler, *Solid State Commun.* **95** (1995) 685.
- [61] R. S. Mulliken, *J. Chem. Phys.* **23** (1955) 1833.
- [62] F. Gao, *Phys. Rev. B* **73** (2006) 132104.
- [63] H. Gou, L. Hou, J.W. Zhang, F. Gao, *Appl. Phys. Lett.* **92** (2008) 241901.
- [64] A. Szymański, J.M. Szymański, *Hardness Estimation of Minerals Rocks and Ceramic Materials*, sixth ed., Elsevier, Amsterdam, 1989.
- [65] V.M. Glazov, V.N. Vigdorovid, *Hardness of Metals*, Izd. Metellurgiya, Moskva, 1989.
- [66] M. Radovic and M. W. Barsoum, *American Ceramic Society Bulletin*, **92** (2013) 20-27.
- [67] M.B. Kanoun, S. Goumri-Said, A.H. Reshak, *Comp. Mater. Sci.* **47** (2009) 491–500.
- [68] W.J. Weber, *Radiation Effects and Defects in Solids* **77** (1983) 295-308.
- [69] F.W. Clinard Jr, D.L. Rohr, and R.B. Roof. , *Nucl. Instrum. Methods Phys. Res. B***1**, 581-586 (1984).
- [70] K. E. Sickafus, L. Minervini, R. W. Grimes, J. A. Valdez, M. Ishimaru, F. Li, K. J. McClellan, T. Hartmann, *Science* **289** (2000) 748-751.

